Marine Geology 417 (2019) 106003

Contents lists available at ScienceDirect

Marine Geology

journal homepage: www.elsevier.com/locate/margo

Quantitative characterisation of contourite deposits using medical CT

Thomas Vandorpe[a,b,*], Tim Collart[a], Veerle Cnudde[a,c], Susana Lebreiro[d], F. Javier Hernández-Molina[e], Belen Alonso[f], Anxo Mena[g], Laura Antón[d], David Van Rooij[a]

[a] Ghent University, Department of Geology, Campus Sterre, building S8, Krijgslaan 281, 9000 Gent, Belgium
[b] Flanders Marine Institute (VLIZ), Wandelaarkaai 7, 8400 Oostende, Belgium
[c] Department of Earth Sciences, Utrecht University, Princetonlaan 8A, 3584CD Utrecht, the Netherlands
[d] Instituto Geológico y Minero de España (IGME), Madrid, Spain
[e] Department of Earth Sciences, Royal Holloway, University of London, Egham, Surrey TW20 0EX, UK
[f] Instituto de Ciencas del Mar (CSIC), Barcelona, Spain
[g] Departemento de Xeociencas Mariñas e Ordenación do Territorio, University of Vigo, Vigo, Spain

ARTICLE INFO

Editor: Michele Rebesco

Keywords:
Medical Computed Tomography (CT)
Contourites
Grain size
Bottom currents
Gulf of Cadiz
Alboran Sea

ABSTRACT

Five sediment cores, retrieved from four different depositional contouritic morphological settings (a sheeted drift, a confined mounded drift, a mounded elongated drift and a plastered drift) from the Northern Gulf of Cadiz and the Alboran Sea have been analysed using medical X-ray computed tomography (medical CT). A quantitative approach has been used, resulting in a workflow that delineates several radio-density ranges based on the Hounsfield Unit (HU) histogram of each core and tracks these ranges throughout the cores. In order to derive the geological significance, the radio-density ranges of all cores have been compared to non-destructive, continuous chemical and physical proxies as well as grain size measurements. The highest correlations occurred between high HU and proxies indicating elevated bottom currents, such as Zr/Al and sortable silt. Additionally, a continuous increase in average HU and inferred bottom current velocities, needed for the creation of the specific contourite setting, could be observed throughout the five cores. Despite imperfections and the requirement of additional research, promising results have been obtained which could improve the detection of diagnostic criteria for contourites. Moreover, the CT data can give more conclusive evidence on the nature of the (contourite) sedimentary sequence boundaries.

1. Introduction

Contourites are defined as sediments deposited or substantially reworked by the persistent action of bottom currents and their accumulation in marine and lacustrine environments can lead to the formation of sedimentary bodies called drifts (Rebesco et al., 2014). Contourites can be classified based on their lithological, sedimentological and morphological characteristics (Rebesco et al., 2005; Rebesco et al., 2014). The lithological content of contourites varies from clay to gravel (Viana et al., 1998; Stow and Faugères, 2008; Verdicchio and Trincardi, 2008) and they can contain biogenic, terrigenous and volcanic compositions, although a combination is ubiquitous (Stow and Faugères, 2008). The sedimentological classification of contourites consists of clastic, calcareous and chemogenic types. The first two categories include muddy, silty, sandy and gravel contourites, while the latter consists of manganiferous and gravel-lag contourites (Stow and Faugères, 2008; Rebesco et al., 2014). The combination of lithological and sedimentological properties resulted in the contourite facies model of Faugères et al. (1984) and Gonthier et al. (1984). The model was updated by Stow and Faugères (2008) and consists of a coarsening and fining-up (bigradational) sedimentary sequence (Fig. 1). Five contourite facies (C1–C5) are part of the typical contourite sequence, while basecut-out (contourites developed on top of a discontinuity) and topcut-out contourites (contourites topped by a discontinuity) are also considered (Fig. 1). The model fits relatively well fine-grained contourites (muddy and silty), but does not fit well sand-rich contourites.

Since the widely-recognized contourite facies model is solely based on sedimentological and lithological criteria, discerning contourites from turbidites within sediment cores has been proven difficult in many cases (Shanmugam, 2000) as both may contain a similar sharp basal (erosional) contact. In addition, vigorous bottom currents may create sandy contourites (Brackenridge et al., 2018), bottom current reworked sands (Mutti and Carminati, 2012; Shanmugam, 2012) or mixed/hybrid turbidite-contourite deposits (Llave et al., 2007; Hernández-Molina,

* Corresponding author at: Slipwaykaai 2, 8400 Oostende, Belgium.
E-mail address: thomas.vandorp@vliz.be (T. Vandorpe).

https://doi.org/10.1016/j.margeo.2019.106003
Received 21 November 2018; Received in revised form 22 July 2019; Accepted 25 July 2019
Available online 30 July 2019

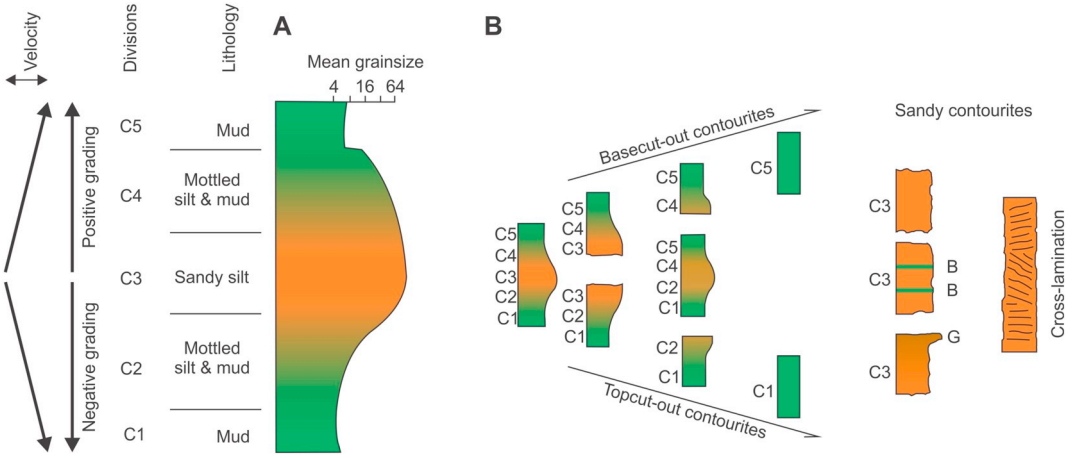

Fig. 1. Bottom current velocity tendency, grain size grading, divisions and lithology of a typical contourite sequence (A) based on the Faugères et al. (1984) and Gonthier et al. (1984) facies model. (B) Adaptations to the basic model, where basecut-out and topcut-out contourites are considered as well as several sandy contourite facies. B: bioturbation, G: gravel horizon. Figure adapted from Faugères and Stow (2008).

2009; Brackenridge et al., 2013; Sansom, 2018), further complicating the distinction between both types of deposits. Recently, Brackenridge et al. (2018) created a new sand-rich contourite facies model based on a dataset originating from sediment cores from the Gulf of Cadiz. Medical X-ray computed tomography (CT) was one of the techniques used to characterize the cores and help set up the model. The CT data were displayed as a high-resolution ($0.2 \times 0.2 \times 0.625$ mm) radio density image, improving the ability to log broad grain size trends, erosional boundaries and sedimentary features. CT data have been used in earlier contourite research to allow high-resolution visualisations of structures within sediment cores (Lucchi et al., 2002; Mulder et al., 2013; Rebesco et al., 2013; Hanebuth et al., 2015; Mena et al., 2018). In contrast, quantitative analysis of the data is still in development. Mena et al. (2015), for example, used ranges of Hounsfield units (HU) to distinguish pelagic, hemipelagic, contouritic, turbiditic and ice-rafted debris layers. By incorporating innovative techniques, such as CT, the contourite facies model can be further developed, allowing a more sustained determination of contourite facies in sediment cores.

This paper focusses on the quantitative analysis of the CT scans from five selected contourite sediment cores in order to identify and characterize the intervals deposited during periods of elevated bottom currents. The goal of this paper is to demonstrate the potential of CT data to analyse sediment cores, ascertain what the quantitative CT data reflect and to verify whether CT scan data may be taken up as an additional diagnostic criterion in the contourite facies model.

2. Study area & sediment cores

In order to compare scans from a range of contourite morphologies, this paper focusses on the medical CT scans of five selected sediment cores from the Gulf of Cadiz and the Alboran Sea (SW Mediterranean Sea; Fig. 2; Table 1). Both areas have been studied in depth (Gonthier et al., 1984; Nelson et al., 1993; Llave et al., 2001; Ercilla et al., 2002; Hernández-Molina et al., 2006; Stow et al., 2013; Ercilla et al., 2016; Hernández-Molina et al., 2016; Juan et al., 2016) and may be considered as the cradle for contourites. Two water masses influence the immediate location of the cores in the Gulf of Cadiz (Fig. 2), North Atlantic Central Water (NACW) and Mediterranean Outflow Water (MOW). NACW flows from west to east and splits up into three branches, one of which enters the strait of Gibraltar. MOW flows out of the Strait of Gibraltar, deviates to the right due to Coriolis forcing and splits up into two main branches (the lower and upper core). The lower core splits up into 3 branches due to the topographic obstacles in the Gulf of Cadiz (Borenäs et al., 2002; García, 2002; Louarn and Morin, 2011). All of the MOW cores and branches follow a mainly north and westwards path. In the Western Alboran Sea, four main water masses are present (Fig. 2; based on Millot (1999) and Ercilla et al. (2016)). The Western Mediterranean Deep Water (WMDW) flows from east to west in the Alboran Sea below 600 m water depth, before being forced upwards closer to the Strait of Gibraltar (Fabrés et al., 2002). Levantine Intermediate Water (LIW) flows along the Spanish margin at water depths of 200 to 500–600 m in a westerly direction (Branckart and Pinardi, 2001). The Winter Intermediate Water (WIW) also flows westwards along the Spanish margin at water depths of 75 to 300 m and has a large seasonal variability (Millot, 2009). The Atlantic Water (AW) is present down to 250 m water depth and enters the Alboran Sea through the Strait of Gibraltar, flowing eastwards and creating a gyre in the Western Alboran Sea (Parilla et al., 1986).

Two cores from the Gulf of Cadiz (Cadiz10_PC06 and GC01) were analysed (Fig. 2). Core Cadiz10_PC06 (hereafter called PC06; 489 m water depth) originates from a plastered contourite drift on the upper continental slope (Hernández-Molina et al., 2006; Hernández-Molina et al., 2014) and is composed of more coarse-grained sediments belonging mainly to the coarse silt and fine sand fractions (Brackenridge et al., 2018). The facies within PC06 can be assigned to the C2–C4 divisions of the contourite facies model (Fig. 1) and display bigradational sequences and erosion surfaces (Brackenridge et al., 2018). Core GC01 (566 m water depth) originates from the Faro-Albufeira drift system (Stow et al., 1986; Llave et al., 2001; Llave et al., 2007), an elongated mounded drift that consists of the incisive Alvarez Cabral moat and a distinct mounded drift part (Llave et al., 2001). GC01 consists of three silty contourites interbedded in muddy contourites (Lebreiro et al., 2018). The origin of the transitions between both facies is ascribed to fluctuations in flow velocities of the MOW, related to millennial-scale palaeoceanographic and climatic changes (Llave et al., 2006; Lebreiro et al., 2018).

Three cores from the Alboran Sea were analysed, namely Sagas K3, Montera PC15 and Montera PC08 (Fig. 2). Cores Sagas K3 (hereafter called K3; 712 m water depth) and Montera PC15 (hereafter called M15; 763 m water depth) were retrieved from the Djibouti confined drift. The drift is located south of the Djibouti Ville Seamount (Palomino et al., 2011), within a region swept by WMDW (López-González et al., 2019; Fig. 2). Core K3 is derived from the mounded part (drift) while core M15 is from the moat of the confined drift. Both cores contain muddy to silty mud contourites, although core M15 contains coarser grains compared to core K3 (Alonso et al., 2014). Core MONTERA PC08 (hereafter called M08) is retrieved from the Tres Forcas sheeted elongated drift within the Alboran Sea (Ercilla et al., 2016). The Tres Forcas drift is located south of the Alboran ridge, within a region under the influence of the WMDW (Fig. 2). M08 is composed of muddy

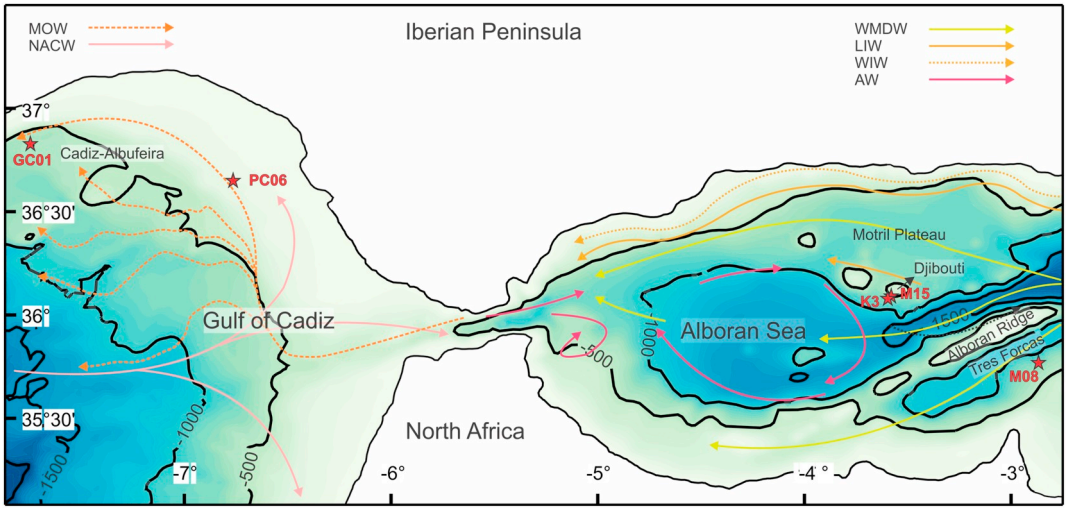

Fig. 2. Location of the cores (red stars) and morphological provinces investigated in this study area. The pathway of the main water masses in the Alboran Sea and Gulf of Cadiz are indicated (based on previous compilations by Ercilla et al. (2016) for the Alboran Sea and by Hernández-Molina et al. (2016) for the Gulf of Cadiz. Original oceanographic references are in those papers). WMDW = Western Mediterannean Deep Water, LIW = Levantine Intermediate Water, WIW = Winter Intermediate Water, AW = Atlantic Water, MOW = Mediterrean Outflow Water, NACW = North Atlantic Central Water. (For interpretation of the references to colour in this figure legend, the reader is referred to the web version of this article.)

contourites (Vázquez and Alonso, 2012).

Together, these five cores make sure that several drift morphologies (confined, elongated mounded, plastered and sheeted) and lithologies (sandy, silty and muddy) are represented within the dataset as well as different sedimentary environments within one contourite drift (moat versus mounded part in the Djibouti contourite drift). As such, a broad range of different depositional contourite settings is analysed.

3. Methods

3.1. XRF

All cores were previously analysed at a resolution of 1 cm using non-destructive continuous X-ray Fluorescence (XRF) core scanning. This was performed with the Avaatech XRF core scanner of the Universitat de Barcelona (Spain), Faculty of Geology. The sediment surface was covered with an ultralene film to avoid contamination. Except for PC06 (where only 10 keV was used), all other cores were scanned at both 10 and 30 keV.

3.2. MSCL

Non-destructive, continuous physical properties measurements had already been performed on cores GC01, M15, K3 and M08 using the Geotek Multi-Sensor Core Logger (MSCL). They were logged at an interval of 1 cm with the magnetic susceptibility and gamma density sensors. M15, K3 and M08 were logged on board of the R/V Sarmiento de Gamboa, while GC01 was logged at IGME Madrid (Spain). The sediment of core PC06 is very loose, resulting in sediment displacements when the core was subjected to MSCL measurements. As a consequence, these measurements are considered not being trustworthy.

3.3. Grainsize

Grain size measurements were performed on all cores. Cores PC06, M15, K3 and M08 were analysed using either a Coulter or a Mastersizer, while sortable silt values, deduced from Sedigraph measurements, were calculated for GC01. These data are legacy data, obtained in the framework of earlier research objectives. Since comparing absolute Coulter, Mastersizer and Sedigraph data yields small-scale differences (McCave and Hall, 2006; Roberson and Weltje, 2014), percentages of grain size classes are used in all further analyses, reducing the error induced by the different grain size measurement techniques.

Core PC06 was subsampled every 2 cm. The samples were treated with hydrogen peroxide to remove the organic matter and kept in a 0.6% sodium hexametaphosphate (calgon) to separate clays before analysis with a Malvern Mastersizer 3000 (Brackenridge et al., 2018). Core GC01 was sampled every 4 cm on average. Organic matter and carbonates were removed with 33% hydrogen peroxide and 0.2 N hydrochloridic acid respectively. The samples were kept in a 0.5% calgon solution to avoid flocculation. The grain size distributions were acquired in the 10–63 μm interval with the Sedigraph Micromeritics III Plus, yielding sortable silt values (Lebreiro et al., 2018). Cores M15, K3 and M08 were subsampled every 10, 7 and 4 cm (on average) respectively. The samples were treated for 1 day with a 50 ml 1 M hydrochloridic acid solution in order to remove the carbonate fraction and with a hydrogen peroxide solution in order to remove the organic matter. Finally, a 2.5% calgon solution was added to the sample and it

Table 1
Metadata of the investigated cores. Their short name (used throughout this paper) is indicated in bold. XRF: X-ray fluorescence scanning; MSCL: multi-sensor core logger; GS: grain size; CT: computed tomography.

Core	Latitude	Longitude	Length	Analyses	Water depth	Main references
Cadiz10_PC06 (**PC06**)	36° 18.27′N	6° 45.86′W	2.4 m	XRF, GS, CT	489 m	Brackenridge et al. (2018)
GC01A-PC (**GC01**)	36° 42.63′N	7° 44.71′W	5.2 m	XRF, MSCL, GS CT	566 m	Lebreiro et al. (2018)
Montera_PC15 (**M15**)	36° 05.43′N	3° 34.81′W	5.9 m	XRF, MSCL, GS, CT	763 m	Alonso (2010) & Palomino et al. (2011)
Sagas K3 (**K3**)	36° 04.94′N	3° 35.59′W	4.5 m	XRF, MSCL, GS, CT	712 m	Alonso (2010) & Palomino et al. (2011)
Montera_PC08 (**M08**)	35° 46.10′N	2° 52.05′W	6.3 m	XRF, MSCL, GS, CT	753 m	Alonso et al. (2014)

Table 2
Summary of the grain size measurements on the five cores.

	PC06	GC01	M15	K3	M08
Organic matter removed	Yes	Yes	Yes	Yes	Yes
Decarbonated	No	Yes	Yes	Yes	Yes
Interval of measurements (μm)	0.06–1000	10–63	0.4–900	0.4–900	0.4–900
Sortable silt	No	Yes	No	No	No
Equipment	Malvern	Sedigraph	Coulter	Coulter	Coulter
Location of analysis	University Barcelona	IGME Madrid	University Barcelona	University Barcelona	University Barcelona

was put into an ultrasonic bath. The characteristics of the grain size measurements are summarized in Table 2.

3.4. Medical X-ray computed tomography (CT)

X-ray CT is a non-destructive technique which allows to visualize and characterize the inner structure of an object in three dimensions based on the variations in X-ray attenuation (Brabant et al., 2011). X-ray images are gathered based on the absorption of X-rays by material, depending on the initial energy, expressed in Beer's law (Cnudde and Boone, 2013). Depending on the energy and detectors used, several resolutions can be obtained ranging from mm- (medical CT scans) to μm-resolution (micro-CT scanners). Typically, the higher the resolution, the smaller the sample must be (Ketcham and Carlson, 2001). Since entire core sections (ranging from 0.5 to 1.5 m) have been scanned in this study, a medical CT scanner was used. Especially since medical scanners allow horizontal scanning and can scan entire sections at once. Given the energies used by the medical CT scanner (120 kV), Compton scattering and to a lesser extent photoelectric effects may play a role in the CT images Ketcham and Carlson, (2001). The Compton effect can be explained as the incident photon colliding with an outer-shell electron and losing energy in this process. The probability of a Compton reaction depends largely on the density of the material and will thus occur more in high-density materials. The photoelectric effect is caused when photons cause an inner-electron to be ejected, releasing another photon with a lower energy. The probability of this event increases when the energy of the incident photon is close to the individual electron binding energies of each shell. As a medical CT scanner with 120 kV has been used in this study, the X-rays are more prone to density changes compared to differences in composition.

Two approaches can be applied when it comes to CT scans: a descriptive (visual) and a quantitative (analytical) approach. The quantitative approach applied in this study makes use of Hounsfield Units (HU). HU is a measure for attenuation coefficients of material in medical CT scans. Distilled water is defined as zero and air as −1000 (Zatz, 1981; Freeman, 2010). HU is dependent upon density/porosity, thickness and the composition (effective atomic number) of the object (Cnudde and Boone, 2013). Consequently, a porous material composed of elements with a higher average atomic number can yield similar x-ray attenuation and therefore similar HU as a more dense material consisting of elements with a lower average atomic number.

All archive halves of the five cores were analysed using the SOMATON definition flash scanner at Ghent University hospital. Due to the rotating source of this scanner, digital slices can be reconstructed based on digital radiographs using the SAFIRE reconstruction software (Grant and Raupach, 2012). A 120 kV step and rotation time of 1 s resulting in a cross-core x and y-resolution of 0.2 mm and an along-core z-resolution of 0.6 mm were set and the images were reconstructed using the “J37s medium smooth” algorithm.

4. Quantitative CT workflow

The quantitative workflow (Fig. 3) was established and executed using Python and R-scripts, which are freely accessible (presented in Supplementary material, S4 and on GitHub; Collart, 2019), ensuring consistency and repeatability in future applications.

In order for the HU to be representative of the sediment analysed in the physical properties and grainsize measurements, a region of interest of 200 by 100 pixels is defined in each slice (Fig. 3a). The region of interest is determined by localizing the two upper corners of the liner and selecting the region in the core center which lies 25 (or 50 for cores PC06 and K3) pixels below the splitting surface (Fig. 3a). This approach also ensures that the considered sediment is free from deformation, typically present along the liner and at the sediment surface. This deformation results from either the coring or the core splitting process. The selection of the region of interest for random spaced slices in each core is presented in supplementary material (S1). To reduce computing time and allow for unbiased evaluation of the model, a train and test dataset, each consisting of 10 million voxels/core, was derived from the regions of interest by random sampling. The frequency distribution (histogram) of the HU in the training set is then established for every core (Fig. 3b).

Gaussian distributions are fitted to every cores' histogram using a Gaussian Mixed Model, allowing the distinction of several components (Fig. 3b). Gaussian Mixed Models are preferred since they are a commonly used CT image segmentation technique (Almeida et al., 2015). The amount of components considered is based on the models' relative goodness of fit measured by the Akaike information criterion (AIC). The AIC allows an assessment of the relative quality of statistical models by assessing the amount of information in the data that is lost by a given model (Akaike, 1998). As soon as only marginal gains are registered when including an additional component, that additional component will not be considered in the Gaussian model (Fig. 3b). Practically: when the curve of the AIC flattens, no additional components are considered (Fig. 3c). A component is characterized by an upper and lower bounding HU (blue lines in Fig. 3b) and contains all sediment that renders voxels with HU in between those bounding values. For each slice, the relative frequency of each component in the region of interest (100 × 200 pixels) is quantified (Fig. 3d). By considering all slices, the variation of the components throughout the core is obtained and is displayed as a percentage plot (Fig. 3e). The histogram for each core, together with its components, is presented in supplementary material (S2).

The variation of the components throughout the core is compared to selected physical, elemental and grain size proxies by applying a principal component analysis (PCA, presented in supplementary material S3). Correlation coefficients were calculated between the core's components and a selective number of proxies, indicating whether a proxy is co-varying with a component or not (Fig. 4). A two-sided *t*-test was performed to asses if the acquired correlation coefficients are significantly different from 0 at a significance level $\alpha = 0.05$. Coefficients with values above 0.05 are not considered for further analyses and are greyed-out in Fig. 4. Furthermore, PCA was used to visualize the variability in the multi-dimensional dataset. The number of proxies considered for this purpose (Table 4) was determined based on several studies regarding diagnostic proxies for contourite deposits (Rothwell and Rack, 2006; Rothwell and Croudace, 2015). For example, sortable silt is a good measure for paleo-bottom current strengths (McCave et al., 1995; McCave, 2008). Also, the Zr/Al ratio can indicate variations in bottom current strength (Bahr et al., 2014). The list is not exhaustive,

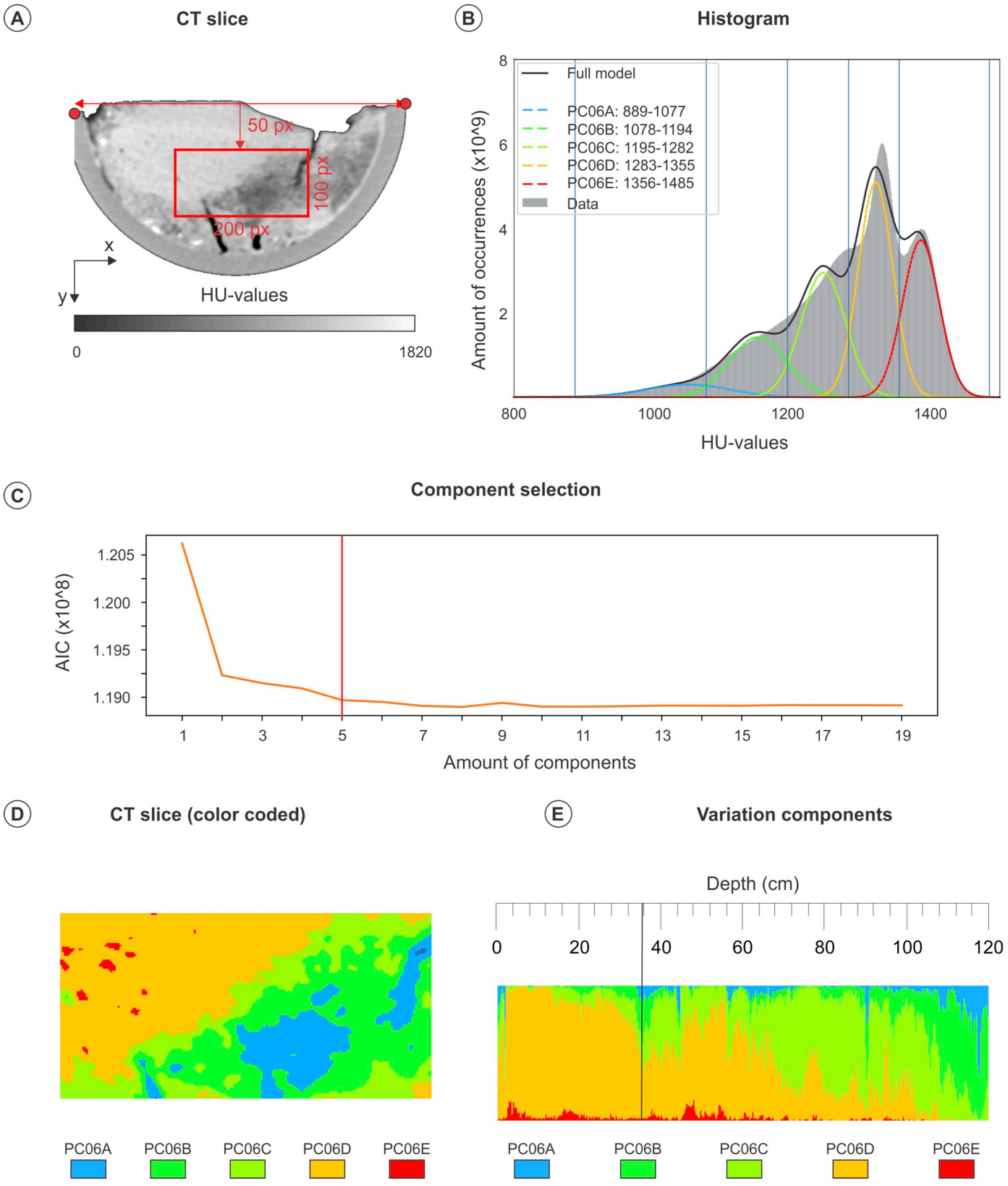

Fig. 3. Overview of the quantitative CT workflow. In this example, the slice at 35.2 cm of core PC06 is used. A. The original slice displayed in grey values (Hounsfield units). The red box indicates the region of interest, 50 pixels below the upper corners (red dots) of the core. B. HU histogram of the integrity of core PC06 with indication of the identified components. Their bounding values are displayed as blue lines and coincide with the crossing of two Gaussian distributions. C. Plot of the Akaike information criteria (AIC) versus the amount of components for core PC06. After 5 components, the curve flattens, resulting in the selection of 5 components for core PC06. D. The slice at 35.2 cm colour coded based on the histogram. E. Overview of the upper 120 cm of core PC06. The black line indicates the position of the slice visualized in parts A and C. (For interpretation of the references to colour in this figure legend, the reader is referred to the web version of this article.)

	PC06A	PC06B	PC06C	PC06D	PC06E
Fe/Al	-0.16	-0.07	-0.28	-0.10	0.35
Ca/Fe	-0.28	-0.47	0.10	**0.65**	-0.28
Ti/Al	-0.29	-0.28	-0.43	0.08	0.45
Al/Ca	0.47	**0.57**	0.24	-0.47	-0.20
Si/Ti	-0.08	-0.22	0.05	**0.59**	-0.39
Ti/Ca	0.16	0.33	-0.27	-0.50	0.37
S/Cl	0.44	**0.53**	0.39	-0.42	-0.31
Zr/AL					
Den					
FP					
MS					
clay	**0.60**	**0.80**	0.38	-0.65	-0.31
silt	**0.59**	**0.79**	0.33	-0.71	-0.21
vf sand	-0.56	-0.66	-0.54	0.40	**0.53**
f sand	-0.51	-0.73	-0.17	**0.74**	0.03
m sand	-0.27	-0.46	0.11	**0.50**	-0.16

	GC01A	GC01B	GC01C	GC01D
Fe/Al	0.41	-0.02	-0.53	0.41
Ca/Fe	-0.08	-0.64	0.14	**0.55**
Ti/Al	0.20	-0.14	-0.50	**0.62**
Al/Ca	-0.25	**0.50**	0.12	-0.53
Si/Ti	-0.40	-0.11	**0.50**	-0.26
Ti/Ca	-0.10	0.61	-0.32	-0.21
S/Cl				
Zr/Al	0.03	-0.22	-0.43	**0.72**
Den	-0.52	-0.28	0.08	0.49
FP	**0.52**	0.28	-0.08	-0.49
MS	-0.17	0.20	0.11	-0.25
m silt	-0.17	-0.25	-0.01	0.37
c silt	-0.08	-0.18	-0.43	**0.74**
vc silt	-0.07	-0.21	-0.48	**0.83**

	M15A	M15B	M15C	M15D	M15E	K3A	K3B	K3C	M08A	M08B	M08C	M08D	M08E
Fe/Al	0.09	-0.09	-0.25	0.22	0.41	0.14	-0.26	0.08	**0.72**	-0.03	-0.31	-0.30	-0.15
Ca/Fe	0.34	0.11	-0.27	-0.19	-0.11	-0.24	0.13	0.25	-0.15	-0.42	-0.20	0.39	0.46
Ti/Al	0.14	-0.11	-0.29	0.24	0.36	0.12	-0.22	0.04	**0.75**	-0.11	-0.39	-0.26	-0.05
Al/Ca	0.22	-0.12	-0.37	0.26	0.37	0.31	-0.14	-0.34	-0.36	0.38	0.38	-0.13	-0.30
Si/Ti	-0.32	-0.04	0.42	-0.06	-0.15	-0.17	0.23	0.02	-0.74	-0.07	0.32	0.36	0.22
Ti/Ca	0.22	-0.12	-0.37	0.26	0.37	0.34	-0.22	-0.30	-0.01	0.39	0.21	-0.29	-0.36
S/Cl	0.21	-0.13	-0.36	0.26	0.37	-0.08	0.16	-0.08	-0.18	0.06	0.12	0.01	0.01
Zr/Al	0.22	-0.11	-0.37	0.25	0.37	-0.02	-0.20	0.25	**0.56**	-0.27	-0.42	-0.10	0.23
Den	-0.71	-0.30	**0.68**	0.34	0.17	0.00	-0.07	0.07	-0.74	-0.23	0.13	0.48	0.49
FP	**0.71**	0.30	-0.68	-0.34	-0.17	0.24	-0.15	-0.14	**0.74**	0.23	-0.13	-0.48	-0.49
MS	-0.61	-0.06	**0.57**	0.12	-0.08	-0.16	0.05	0.18	**0.55**	0.07	-0.35	-0.15	-0.20
Clay	-0.16	0.07	0.36	-0.24	-0.46	-0.14	0.14	0.01	0.10	0.25	0.01	-0.16	-0.25
Silt	0.30	0.01	-0.19	-0.10	-0.20	0.27	-0.15	-0.20	-0.07	-0.20	0.01	0.13	0.18
Sand	0.10	-0.06	-0.30	0.25	0.40	-0.21	0.00	0.34	-0.13	-0.21	-0.07	0.15	0.32

Fig. 4. Overview of the correlation coefficients. The greyed-out coefficients are not significant at $\alpha = 0.05$. The green values all surpass 0.50. Den = Gamma Density; FP = Fractional Porosity; MS = magnetic susceptibility; vf sand = very fine sand; f sand = fine sand; m sand = medium sand; m silt = medium silt; c silt = coarse silt: vc silt = very coarse silt. (For interpretation of the references to colour in this figure legend, the reader is referred to the web version of this article.)

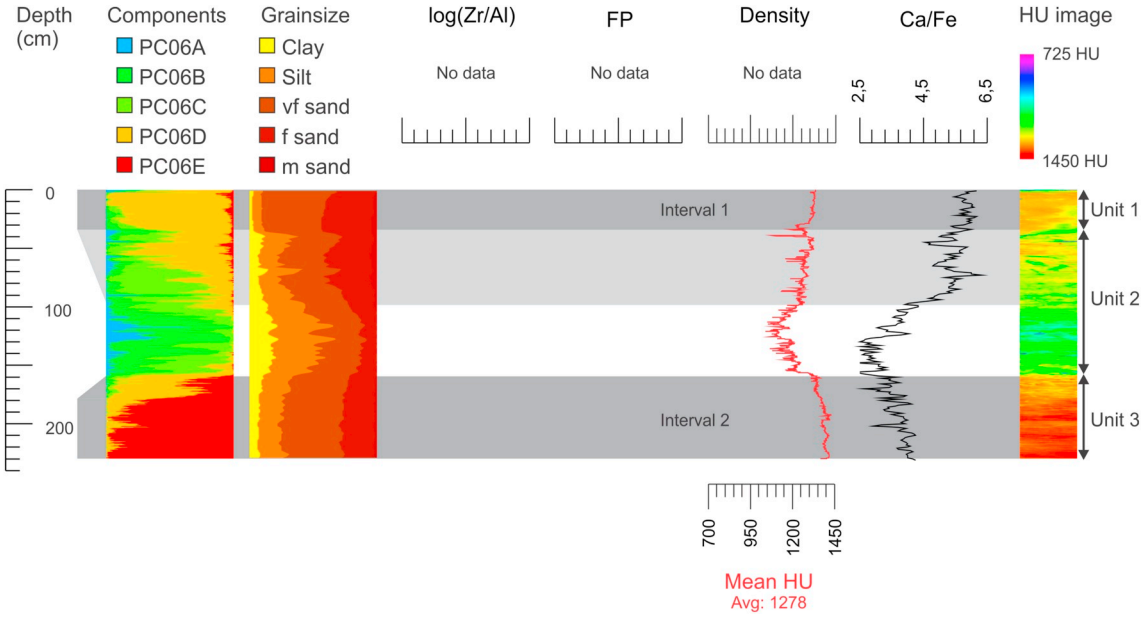

Fig. 5. Overview of core PC06 displaying from left to right the components percentage plot, the grain size classes percentage plot, the variation in log(Zr/Al), fractional porosity (FP), Gamma density, mean HU and Ca/Fe as well as the HU image. The grey intervals denote periods of inferred elevated bottom currents and the grey triangles on the left indicate gradational boundaries. The units defined by Brackenridge et al. (2018) are indicated by the double arrows on the right.

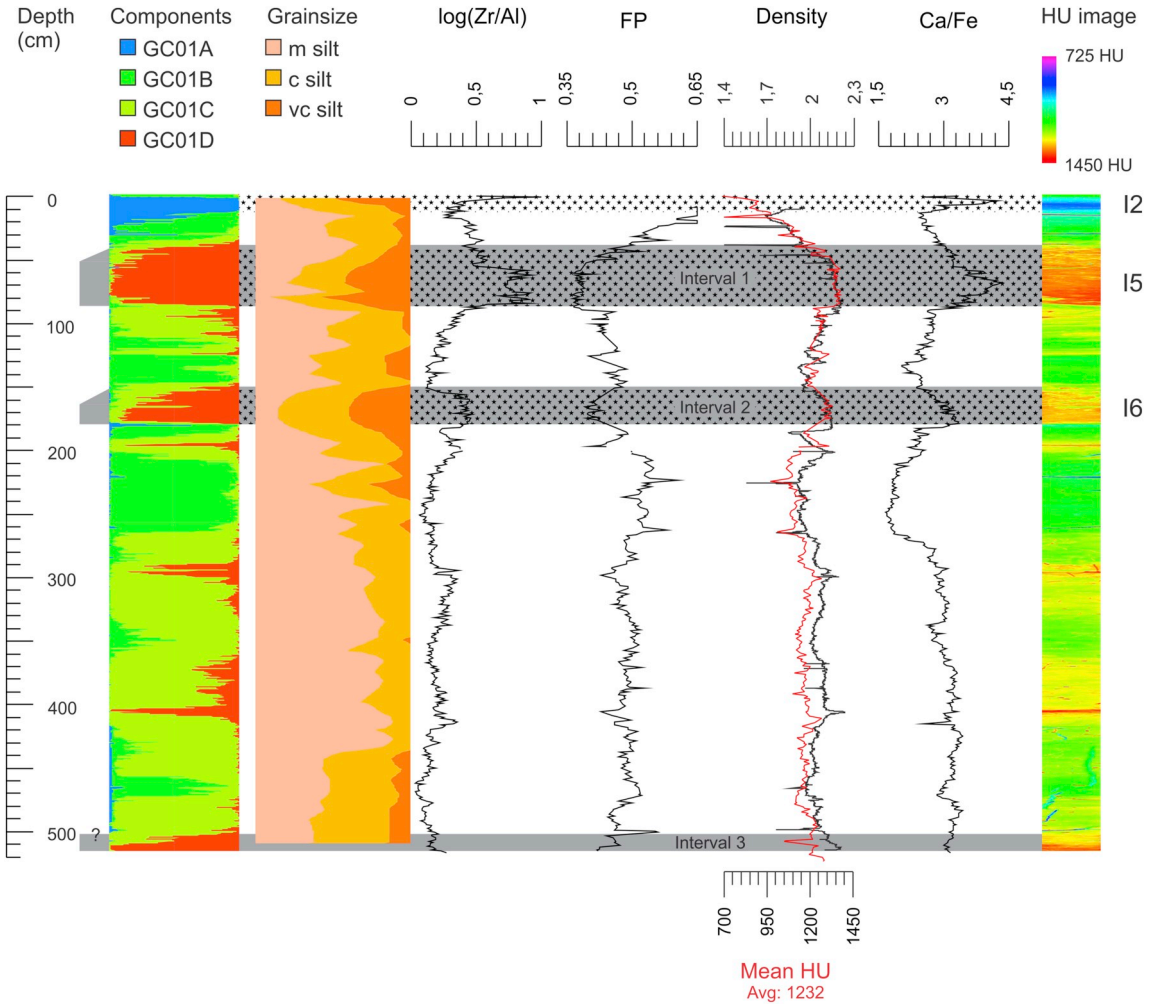

Fig. 6. Overview of core GC01 displaying from left to right the components percentage plot, the grain size classes percentage plot, the variation in log(Zr/Al), fractional porosity (FP), Gamma density, mean HU and Ca/Fe as well as the HU image. The grey intervals denote periods of inferred elevated bottom currents and the grey triangles on the left indicate gradational boundaries. The black dotted intervals are silty contourites I2, I5 and I6 defined by Lebreiro et al. (2018).

but merely sums up the most relevant proxies.

The CT scans were used to render HU images, displayed in Figs. 5 to 9. An HU image is created by averaging each 100 HU in the y-direction (Fig. 3a) of the region of interest of each slice and plotting this on the x-scale. By combining all slices (along-core), an image is generated displaying the average HU in the y-direction along an xz plane. The colours of the HU image are determined by applying a rainbow colour scale with 725 as lower and 1450 as upper boundary. These bounding values resulted in a colour scale allowing the optimal visualization of (sharp) boundaries, characterized by large changes in HU. Important to keep in mind is that due to the different coring devices, the subtle differences in preservation of the cores and the diameter and composition of the liner, the same sediment (composition, porosity, compaction) can appear slightly different (colour-wise) in the various cores.

5. Results

5.1. CT components and intervals

The components of all cores were discerned based on the earlier described workflow (visualized in Fig. 3). As a result, cores PC06, M15 and M08 have five, core GC01 four and K3 three components (Figs. 5 to 9). The CT components of each core are labelled from A to C/D/E (depending on the amount of components).

Overall, core PC06 contains the highest HU of the five cores (on average 1278), resulting in mostly red to orange colours in the HU image and components plot (Fig. 5). The core can roughly be divided into 3 intervals: from the bottom to 156 cm containing very high HU (belonging to components PC06D and PC06E), from 156 cm to 100 cm containing mostly lower HU (belonging to components PC06A, PC06B and PC06C) and from 100 cm to the top containing moderately high HU (components PC06C and PC06D). Around 156 cm and between 100 and 35 cm, a gradual transition between two intervals is present (Fig. 5).

Core GC01 contains high HU as well (average 1232), resulting in mostly green and orange colours in the HU image and components plot (Fig. 6). The core consists of several intervals with higher HU (part of component GC01D): 520 to 500 cm, 420 to 400 cm, 315 to 290 cm, 175 to 150 cm and 100 to 40 cm. The intervals 420 to 400 cm and 315 to 290 cm have rather small peaks where high percentages of the GC01D are observed (1–2 cm only) and are therefore not further considered. The other intervals on the other hand have sustained high percentages of GC01D (for at least 10 cm) and are indicated in grey (Fig. 6). The upper boundaries of the upper two intervals display a relatively sharp lower boundary (Fig. 6).

Core M15 is composed of sediments characterized by moderate to low HU (average 1018), resulting in overall greenish and blue colours in the HU image and components plot (Fig. 7). The core contains three intervals with higher HU (part of components M15D and M15E). These are positioned between the bottom of the core and 560 cm, from 405 to 380 cm and from 135 cm to 15 cm. The boundaries at 135 and 380 cm

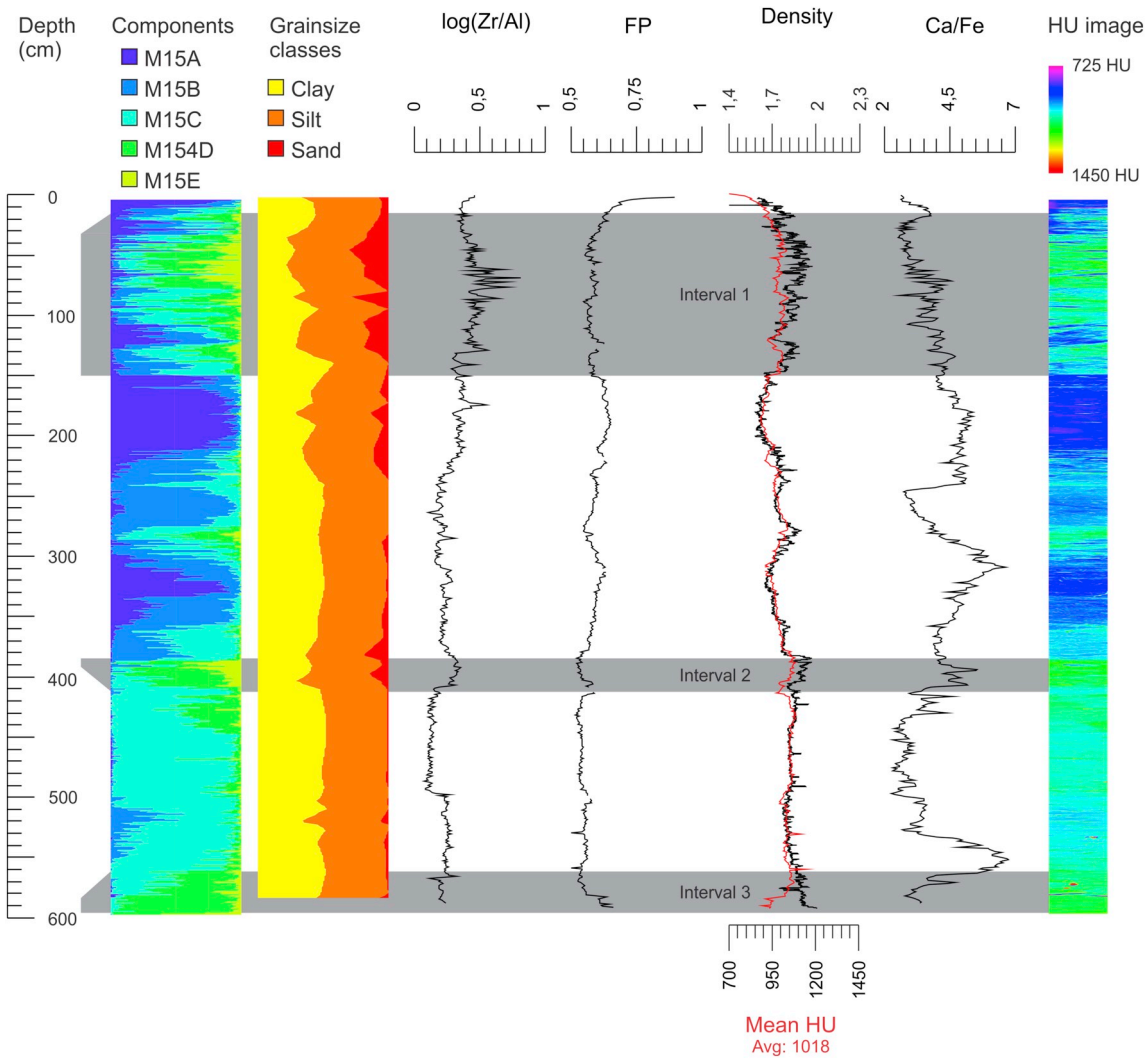

Fig. 7. Overview of core M15 displaying from left to right the components percentage plot, the grain size classes percentage plot, the variation in log(Zr/Al), fractional porosity (FP), Gamma density, mean HU and Ca/Fe as well as the HU image. The grey intervals denote periods of inferred elevated bottom currents and the grey triangles on the left indicate gradational boundaries.

are sharp ones, those at 15, 405 and 580 cm are gradual.

Core K3 mainly consists of moderate to low HU (average 988), resulting in blue and green colours in the HU image and components plot (Fig. 8). One interval (240 to 210 cm) contains higher HU and is mostly composed of component K3C. This interval contains a sharp upper boundary and a gradual lower one. The remainder of the core is mostly composed of variations of K3A and K3B (Fig. 8).

Core M08 is composed of sediments characterized by the lowest HU of all five cores (an average of 824) resulting in purple and blue colours in the HU image and components plot (Fig. 9). Two intervals with higher HU are discerned: from the bottom to 600 cm and from 250 to 120 cm containing mostly the blue components M08E and M08D. The lower interval has a gradual upper boundary, as has the lower boundary of the upper interval. The upper boundary of the upper interval is rather sharp (Fig. 9).

Besides the HU image and components plot, several other proxies are plotted on Figs. 5 to 9. Since contourite deposits are the focus of this paper, delineating intervals resulting from elevated bottom currents is key. Consequently, the grain size classes have been plotted for all cores on their respective figs. A plot of logarithmic values of Zr/Al is included as well, since Zr/Al is a good indicator for bottom current velocities in the Gulf of Cadiz (Bahr et al., 2014). Logarithmic values of Zr/Al are preferred since they better reflect changes without affecting the relative variations. This is due to the fact that logarithmic ratios are less prone to dilution effects in the interpretation of compositional changes and surpass the inherent non-linearity between element concentrations and counts/relative intensities (Weltje and Tjallingii, 2008). Additionally, fractional porosity, density, mean HU and Ca/Fe are plotted on all core figures (Figs. 5 to 9) as well, allowing a visual verification of the correlation between core components and proxies.

5.2. Correlation matrix

The correlation coefficients (Fig. 4) between the proxies (Table 4) and the CT components (Table 3) have been calculated to quantify the correlations. The coefficients are a measure for the covariation of both curves and can indicate whether a certain proxy might be related to that component or not.

Core PC06 contains many high correlations with grain size fractions (Fig. 4). Components PC06A and PC06B show high correlations with the clay and silt fractions (between 0.59 and 0.80). The opposite is true for their correlations with the sand fractions: they are all negative. PC06D displays high correlation coefficients with the fine and medium sand fractions (0.74 and 0.50 respectively), while PC06E has a high correlation with the very fine sand fraction (0.53). Some high correlation coefficients with XRF-proxies are observed (indicated in green in

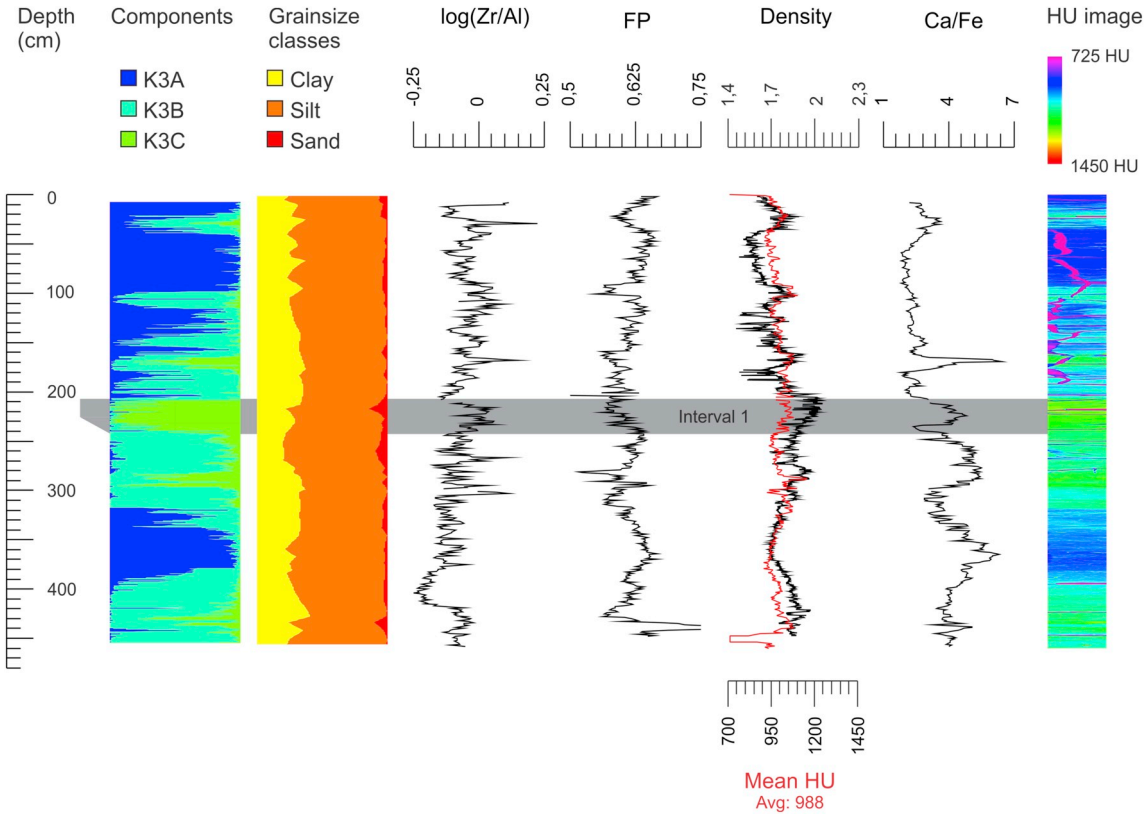

Fig. 8. Overview of core K3 displaying from left to right the components percentage plot, the grain size classes percentage plot, the variation in log(Zr/Al), fractional porosity (FP), Gamma density, mean HU and Ca/Fe as well as the HU image. The grey intervals denote periods of inferred elevated bottom currents and the grey triangles on the left indicate gradational boundaries.

Fig. 4), but they are less pronounced compared to those with the grain size classes.

Core GC01 has some remarkable high correlations between GC01E and several XRF-proxies. The most pronounced one is present between Zr/Al and GC01D (0.72). Also, the high coefficients between GC01D and the coarse and very coarse silt fractions (0.74 and 0.83 respectively) are noteworthy.

Component M15A has a high correlation with fractional porostiy, while M15C shows a high correlation (0.68) with gamma density. For all XRF-proxies, very low coefficients are observed (Fig. 4). Component M15E has a moderately high correlation coefficient with the percentage of sand (0.40), the highest coefficient with one of the grain size classes.

Core K3 does not have high positive or negative correlations with proxies (Fig. 4). From the grain size classes, the highest correlation is observed between K3C and the percentage of sand (0.34).

M08 displays numerous positive and negative correlations of M08A with many XRF-proxies, especially Fe/Al (0.72). M08A also has a high correlation with fractional porosity (0.74). Of the grain size classes, the highest correlation coefficient is observed between M08E and the sand fraction (0.32).

6. Discussion

6.1. Quantitative CT workflow

Several factors may cause uncertainties in establishing the HU of a voxel and induce errors in the quantitative workflow. Additionally, as with any principal component analysis, spurious correlations may cause misguided interpretations. An assessment of these errors is discussed below, in order to validate the workflow.

6.1.1. Partial volume effect

The partial volume effect causes voxels to have HU that are an average of the different elements present within that voxel (Ketcham and Carlson, 2001), resulting in the possible placement of this voxel in the wrong component and inducing a small error. The vast majority of the wrongly classified voxels will occur at the boundaries between two components. The extent of this error is difficult to assess, as higher resolutions are required to verify the content of the voxel. However, given the limited amount of components (3–5, depending on the core) and the high number of voxels within the region of interest (20000) of each slice, the amount of voxels that are assigned to a wrong component due to this error will be minor and not change the overall trends.

6.1.2. Single thresholding

Single thresholding is a technique that allows delimiting components in a histogram by applying one strict lower and upper boundary. Single thresholding cuts away the percentages belonging to the lowest and highest HU and hence potentially induces an error. In order to assess the extent of this single thresholding error, the misclassification probability for each slice has been calculated. The misclassification probability is a measure for the possibility of a given voxel being wrongly classified into a certain category. The probability results from the assignment of a voxel to the component with the highest probability, although a smaller chance remains that it belongs to another component. E.g., at the boundaries of two components, the probability of a voxel belonging to another component is not zero, resulting in a misclassification probability. The average of this probability for each core is between 16.76% (PC06) and 20.97% (M08) (Table 5), indicating that the Gaussian distributions capture at least 79% of the correct voxels (averaged per core). Consequently, the errors remain acceptably low and the general pattern will not be obscured because of single thresholding.

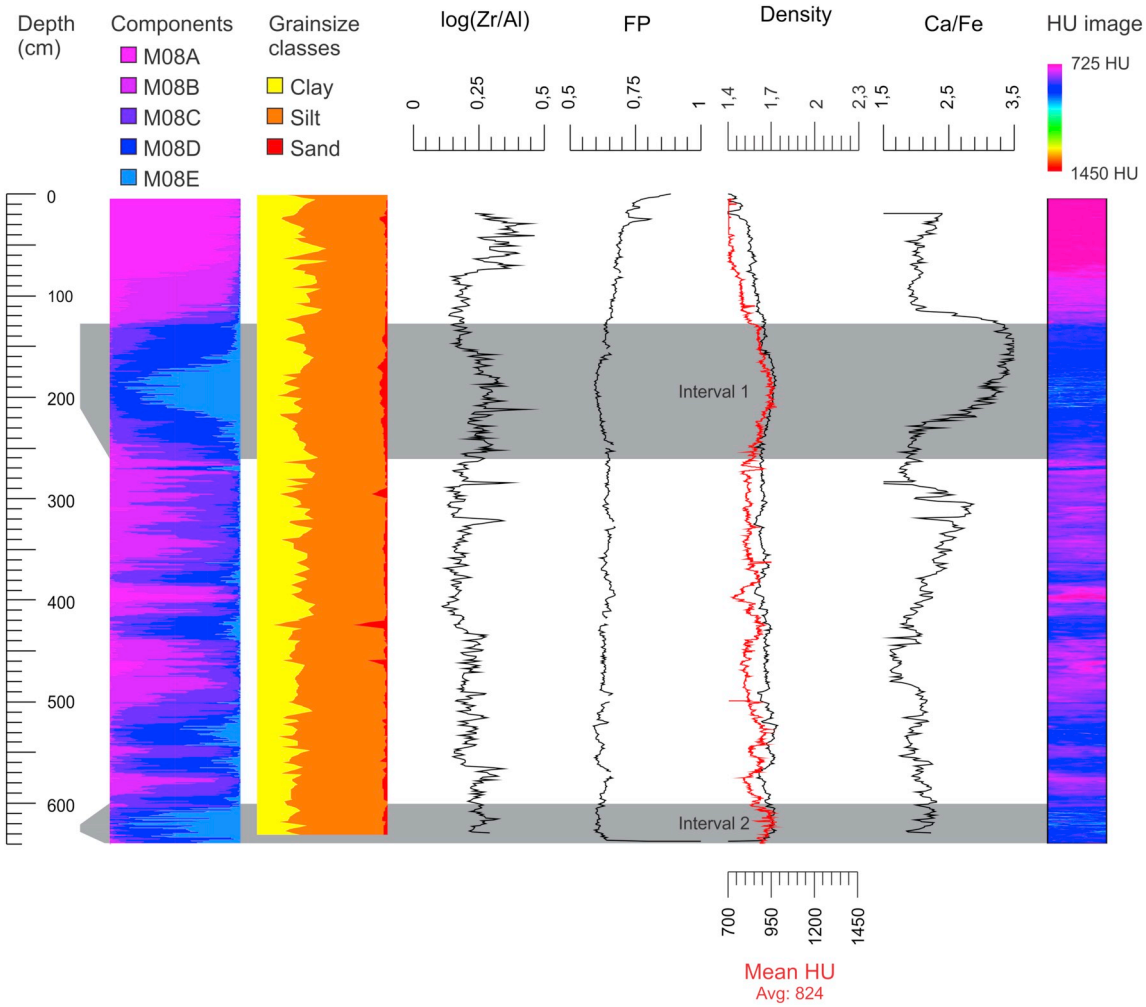

Fig. 9. Overview of core M15 displaying from left to right the components percentage plot, the grain size classes percentage plot, the variation in log(Zr/Al), fractional porosity (FP), Gamma density, mean HU and Ca/Fe as well as the HU image. The grey intervals denote periods of inferred elevated bottom currents and the grey triangles on the left indicate gradational boundaries.

6.1.3. General versus core model

In order to make an overall comparison between the five contourite cores and deduce common components for contourite cores, general components (for all 5 cores) would be the optimal choice. A pool (general) model has been created based on the HU of the regions of interest of all five cores combined and compared to the individual core models (supplementary material, S2). The middle part of the pool model (HU between 850 and 1250) is severely smoothened due to the presence of a large amount of sediment of the different cores, making the deduction of Gaussian components more difficult and creating higher misclassification probabilities. Indeed, for 4 out of 5 cores, the average misclassification probability rises between 2.09% and 5.20%. Only for core M08, the average probability decreases by 5.02% (Table 5). This is due to the fact that core M08 nearly entirely constitutes the lower HU parts of the pool model and consequently does not render higher misclassification probabilities. The average increase in misclassification probability of 1.88% (3.61% when ignoring core M08, which is an increase of nearly 20%) with the pool model indicates that the general components fit the individual cores less. Consequently, the individual core models are preferred.

Varying core diameters and liner materials will result in different absorption ratios from core to core, hampering the application of a pool model or comparing data between cores when a core model has been applied. In this study, all cores have the same liner diameter, 0.8 cm, which only leaves a possible error due to liner material differences. Since all liners are composed of dense plastics (PVC), the error will remain acceptably low, allowing core-to-core component comparisons. For future analyses, cores with the same liner material and diameter are preferred as well, ensuring the elimination of such errors.

Table 3
Bounding HU of the different components of each core.

Core	Component A	Component B	Component C	Component D	Component E
PC06	889–1077	1078–1194	1195–1282	1283–1355	1356–1485
GC01	855–1080	1081–1201	1202–1299	1300–1473	
K3	749–933	934–1004	1005–1081	1082–1170	1171–1359
M08	814–994	995–1158	1159–1339		
M15	596–745	746–802	803–860	861–911	912–1027

Table 4
Overview of the continuous and non-destructive MSCL and XRF proxies, as well as the grain size measurements, used in this study. These proxies are used to compare the CT-components to (Fig. 4).

Proxy	Application	References
Fe/Al	Anoxic bottom water	Spofforth et al. (2008)
Ca/Fe	Terrigenous input variability	Nizou et al. (2011)
Ti/Al	Aeolian input variability	Jiménez-Espejo et al. (2007)
Al/Ca	Terrigenous input variability	Nizou et al. (2011)
Si/Ti	Biogenic silica variability	Agnihotri et al. (2008)
Ti/Ca	Terrigenous input variability	Henrich et al. (2010), Tjallingii et al. (2010)
S/Cl	Organic matter variability	Thomson et al. (2006)
Zr/Al	Bottom current intensity	Bahr et al. (2014)
Gamma density	Sediment bulk density	Schultheiss and Weaver (1992)
MS	Glacial/interglacial cycles	Rothwell and Rack (2006)
Grain size	Sedimentary processes, sorting	McCave et al. (1995)
Sortable silt	Paleo-current strength	McCave et al. (1995)

Table 5
Misclassification probabilities for both the core and general model for each core. The fourth column indicates the differences between the core and general model.

Core	Core model	General model	Difference
PC06	16.76%	21.64%	−4.88%
GC01	17.60%	22.80%	−5.20%
M15	19.99%	22.08%	−2.09%
K3	19.29%	21.54%	−2.25%
M08	20.97%	15.95%	+5.02%
Average	18.92%	20.80%	−1.88%

6.1.4. Spurious correlations

Caution has to be taken when inferring causal relationships from the correlation coefficients in Fig. 4 as spurious correlations may arise. Spurious correlations show a high co-variance between two causally unrelated proxies and are a side-effect of compositional data analysis (Pawlowsky-Glahn and Buccianti, 2011). Such spurious correlations might be present in the correlation matrix and consequently, the geological significance of the correlations should always be verified. Two examples are discussed below.

Some of the highest (positive and negative) correlation coefficients within the matrix occur between components of core PC06 and its grain size data (Fig. 4). These grain size data (Fig. 5) indicate that coarser grains are related to the components with high HU (PC06D and CP06E) and finer grains to the low HU components (PC06A and PC06C). This is evidenced in the PCA plot of core PC06 (supplementary material, S3): the loading vectors of PC06D and PC06E align with those of the percentage of fine sand and the percentage of very fine sand, respectively. In contrast, the PC06A and PC06B loading vectors are closely related to the percentages of silt and clay. Consequently, this should indicate negative correlation coefficients between clay/silt and components PC06D/E and between components PC06A/B and the sand fractions. These values can be observed in the correlation matrix (Fig. 4): coefficients down to −0.73 between the sand fractions and PC06A/B and coefficients down to −0.71 between PC06D/E and clay/silt. This is the first example indicating that coefficients within the matrix are not spurious and can be used for geological purposes.

A second example is deduced from the coefficients of the geochemical data. If the discerned CT components contain geological information, a consistent (simultaneously in- and decreasing values) change of the correlation coefficients between two proxies indicating the same geological parameter is expected. Both Al/Ca and Ti/Ca can be used to infer changes in terrigenous input (Henrich et al., 2010; Tjallingii et al., 2010; Nizou et al., 2011). A graphical presentation of the correlation coefficients of these proxies indicates that the coefficients indeed change consistently (except for GC01D): when moving on to the next component and the coefficient for Al/Ca goes up/down, the coefficient for Ti/Ca does as well (Fig. 10). This example also indicates non-spurious relations and proves that the coefficients can be used for geological and sedimentological studies.

The aforementioned examples indicate that correlation coefficients of Fig. 4 can be considered reliable and may be used for further deductions. Some correlations have to be interpreted with caution though as spurious correlations may be present.

6.2. Bottom current strength and contourite deposits

6.2.1. Bottom currents and high Hounsfield units

The correlation between grain size and bottom current velocities is well established. Higher bottom current intensities result in winnowing of fine particles and eventually the deposition of coarser grains (McCave and Hall, 2006; Stow et al., 2009; Mulder et al., 2013). Especially sortable silt values are a good parameter for bottom current variations (McCave et al., 1995; McCave, 2008). Several observations indicate a link between high HU components and sediments resulting from stronger bottom currents. These observations are:

1. Cores GC01, M15, K3 and M08 all have the highest correlation coefficients between their highest HU component (GC01D, M15E, K3C and M08E) and the coarsest grain size class, being the percentage of very coarse silt for GC01 and the percentage of sand for M15, K3 and M08 (Fig. 4). Also for core PC06, the two components with the highest HU (PC06D and PC06E) have high correlation coefficients with the percentages of sand fractions. This link between high HU component and coarser grain sizes can also be observed in Figs. 5 to 9 where intervals of increasing percentages of coarser grain sizes correspond to intervals of high HU components and higher average HU (these intervals are indicated in grey). Since coarser grains in sediment drifts result from faster-flowing bottom currents, a link between high HU components and faster-flowing bottom currents can be inferred.
2. The three intervals with the highest percentages of GC01D are indicated in grey (Fig. 6). The upper interval neatly corresponds to silty contourite I5 and the intermediate interval to silty contourite I6, both identified by Lebreiro et al. (2018). Since I5 and I6 are both considered as “fast-contourites” (15.5 cm/s) opposed to “slow-contourites” (13 cm/s) occuring throughout most of the remainder of the core (Lebreiro et al., 2018), the intervals also support the link between faster-flowing bottom currents and sediments of higher HU. Silty contourite I2, identified between 0 and 13 cm (Lebreiro et al., 2018) is not observed in the CT data. This may be due to the fact that the upper parts of the core were distorted (collapse of the sediment due to laboratory analyses), which rendered the CT data in that part of the core inusable. The CT data indicate a possible additional “fast-contourite” in the lowest parts of the core (520–500 cm) with accompanying increasing densities. A deeper sediment core is needed though to confirm the presence of this contourite.
3. The HU of core M15 are on average higher than those of K3 (Figs. 7 & 8). Moreover, the sediment of core M15 is characterized by higher mean grain sizes compared to core K3 (16 μm versus 8 μm; Alonso et al. (2014)). These authors linked the overall higher mean grain sizes of core M15 with respect to core K3 to faster flowing bottom currents in the moat (M15) compared to the drift itself (K3). Consequently, the overall higher HU of core M15 may result from faster-flowing bottom currents as well.
4. Although plastered drifts are classified as sheeted drifts - theoretically shaped by relatively low-velocity currents (Rebesco et al., 2014) - the location of PC06 close to the Strait of Gibraltar (Fig. 1)

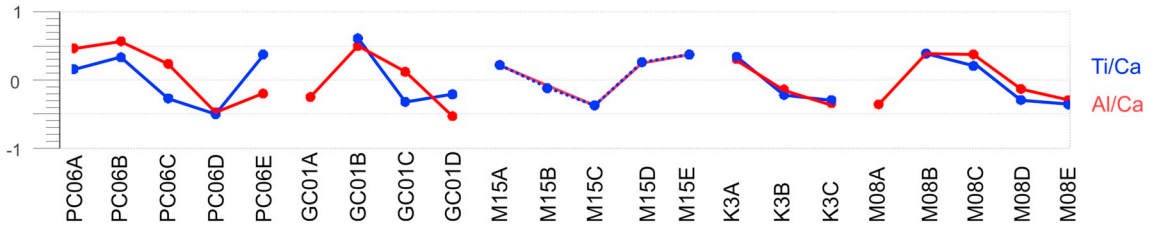

Fig. 10. Variation of the correlation coefficients of Ti/Ca and Al/Ca for the five cores. Coefficients characterized by *p*-values exceeding 0.05 are not taken up in this figure.

and its sandier composition compared to average plastered drifts infer faster-flowing bottom currents were necessary for its creation. Moreover, the core is located in the lower part of a large plastered drift close to the middle slope terrace (García et al., 2009), where high bottom current velocities have been measured, between 10 and 50 cm/s (Sánchez-Leal et al., 2017). As such, more vigorous bottom currents were needed for the build-up of the plastered drift containing PC06 compared to average fine-grained mounded drift deposits (typically between 10 and 30 cm/s), which itself require higher velocities compared to sheeted drift deposits (below 10 cm/s) (Stow and Faugères, 2008; Stow et al., 2009). Therefore, combining the average HU of the five cores (Figs. 5 to 9) also supports the relationship between bottom currents and HU. Indeed, a progressive increase in average HU is noticed for the studied contourite cores when ranging from sheeted (824 for M08) to mounded (988 for K3, 1018 for M15 and 1232 for GC01) and eventually the plastered drift (1278 for PC06).

5. A high correlation between the Zr/Al ratio and GC01D is observed (Fig. 6) with a correlation coefficient of 0.72 (Fig. 4). Bottom currents are known to increase the Zr/Al ratio in marine sediments from the Gulf of Cadiz (Bahr et al., 2014; Lebreiro et al., 2018). The Zr/Al ratio represents the relative enrichment of heavy minerals - like zircon and barite – in marine sediments due to winnowing under higher bottom currents (Pedersen et al., 1992). The relatively high atomic number of zircon (40) compared to aluminium (13), will also cause higher X-ray attenuation coefficients and thus HU. This is due to the fact that the average atomic number of the constituting elements is the most important factor controlling the X-ray attenuation coefficient - and hence HU - of a voxel in sediments containing elements with higher atomic numbers like zircon (Cnudde and Boone, 2013). Consequently, increased percentages of GC01D (high HU component) may thus indicate periods when more Zr remained in the sediment, caused by the winnowing effect of faster-flowing bottom currents.

These five observations indicate that the highest HU in the five cores can be caused by faster flowing bottom currents at the time of deposition and support the idea of a causal link. A possible explanation could be that coarser grains can cause denser sediments (as already observed in some Patagonian fjords for example (Bertrand et al., 2012)), which itself renders higher HU. The latter is evidenced in Figs. 5 to 9 where a near perfect co-variation and overlap exist between the gamma density and mean HU curves. Similar observations were also already reported by Orsi and Anderson (1999).

6.2.2. *Hounsfield units (HU) and bottom current variability*

CT scans may provide information on the nature of the physical changes between contourite sedimentary sequences. They may indicate whether the changes in bottom current intensity, translated into the discrepant HU of the sediment, were rather abrupt or gradual and help in the identification of bigradational, basecut and topcut-out contourites (Fig. 1; Stow et al., 2002; Stow and Faugères, 2008; Stow et al., 2013). The advantage of the HU image compared to visual observations is twofold. First, the medical HU image has a high resolution (0.625 mm in the *Z*-direction), allowing a detailed visualization of the boundaries. Secondly, boundaries between two units with similar colours (visually) are hard to perceive (e.g. Rebesco et al., 2004). If discrepant HU are present between the two units, the boundary can be visualized with the HU image nonetheless.

Core PC06 consists completely out of C2 to C4 contourites and three sedimentological units with sharp boundaries had already been defined (Fig. 5) by Brackenridge et al. (2018). Amongst other, these authors based their distinction on changes in grain size. The CT data indicate the presence of two intervals of faster bottom currents, discerned based on the variation of the components. The lower boundary of interval 1 differs from the unit-boundary discerned by Brackenridge et al. (2018). The difference is explained by the inferred gradational sequence boundary (Fig. 1), observed in both the CT data and grain size data (Fig. 5). Indeed, component PC06C decreases and PC06D increases gradually going from unit 2 to 1 (from 100 to 35 cm depth). Consequently, defining the exact location of the lower boundary of interval 1 is difficult and a gradual boundary should be defined. Although the upper boundary of interval 2 is sharper, the grain size and component data still indicate a rather gradual change (between 180 and 160 cm depth). Similarly, a gradational boundary is proposed as well (Fig. 5).

In core GC01, the CT data identified two of the three silty contourites described by Lebreiro et al. (2018). They consist of bioturbated muds coarsening upwards into sandy silt eventually fining upwards again (Lebreiro et al., 2018), making them prime examples of bigradational sedimentary sequences. The CT data indicate that the upper boundary of silty contourites I5 and I6 are indeed gradational (triangle in Fig. 6). However, the lower boundary of both contourites seems to display a sharp contact. The difference between both interpretations may result from the resolution difference between grain size (4 cm on average) and CT data (0.625 mm), allowing a better assessment of the boundary based on CT data. Consequently, both I6 and I5 can be classified as basecut-out contourites (Fig. 1). The boundary of the lowermost interval is not fully displayed and can therefore not be classified. A deeper core is required to gain insight in its full boundary.

Cores M15 and K3 were retrieved from the Djibouti Ville drift and consist of muddy and silty contourites. Alonso et al. (2014) attributed the sharp grain size changes to substantial bottom current accelerations and decelerations with faster flowing currents in the moat (core M15). Similar to cores PC06 and GC01, intervals of higher HU and coincident higher amounts of silt and sand can be interpreted as resulting from higher bottom currents (indicated in grey in Figs. 7 & 8). In core M15, three such intervals can be discerned. The upper interval can be classified as a basecut-out contourite, while the intermediate interval as a topcut-out sequence (Fig. 7). The lower interval has a gradational upper boundary. Since its lower boundary is not present within core M15, the type of contourite cannot be determined. In core K3, one interval can be distinguished. This interval consists of a gradational lower boundary and a sharp upper one. It is therefore classified as a topcut-out contourite. This interval shows remarkable similarities in both boundaries and thickness to the middle interval identified in M15, indicating it could be deposited at the same time. Absolute datings of the sediment are needed though to confirm or refute this interpretation.

In core M08, no contourite sedimentary sequences have been

determined independently. Also, the variation in grain size classes is less pronounced (Fig. 9). These two criteria hamper the identification of sequence boundaries. Based on the data presented in Fig. 9, two intervals with higher HU (260 to 120 cm and 600 cm to bottom) can be identified. The upper interval has a gradational lower and a rather sharp upper boundary (Fig. 9), identifying it as a topcut-out sequence (Fig. 1). The lower interval displays a gradational upper boundary. Its lower boundary is not entirely present within the core, but suggests a gradational lower boundary as well. A deeper core is required to confirm this interval as a bigradational sedimentary sequence.

7. Conclusions

Both qualitative and quantitative analyses of CT scans of contourite cores are very promising techniques in marine sedimentary facies analysis. CT data are complementary to the sedimentological and lithological data used for (contourite and turbidite) facies description and must thus be regarded as an additional tool for facies identification. Where the qualitative (visual) method is being used already as an enhanced, high-resolution image; the quantitative method is novel. The strength of the quantitative method described in this paper lies in its ability to match higher HU to proxies related to stronger bottom currents. As such, the description of contourite sedimentary sequences in sediment cores can be improved, especially since acquiring CT scan data is a very cost- and time-effective method compared to geochemical, physical and textural data acquisition. Consequently, CT data should be used to describe contourite facies and may improve their recognition in sediment cores.

To evaluate the potential of CT scans for the quantitative description of contourite deposits, five selected sediment cores have been analysed, all from different drift morphological settings (plastered, mounded and sheeted drifts) and with a different texture (sand, silt and clay). This renders the dataset sparse and is the main factor why caution has to be taken with these initial results. Additional cores have to be analysed in order to substantiate the hypothesis. Besides analysing additional sediment cores from similar and other contourite drift settings, the method put forward will also benefit from the analysis of sediment cores from turbidite settings. Turbidites also contain intervals deposited by elevated (downslope) gravity currents (Southard and Cacchione, 1975; Shanmugam, 2008; Piper and Normark, 2009; Rebesco et al., 2014). Consequently, the analysis of turbidite cores with the same method would allow assessing whether the method is suitable for contourite cores only or whether turbidite cores also display the same CT characteristics. In addition, the presence of bioturbation in contourite cores is well established, while in turbidites, this is less the case (Rodríguez-Tovar and Hernández-Molina, 2018). A (visual) assessment of the bioturbation in sediment cores based on CT images may also yield valuable information on the nature of the sediment and may be incorporated in the contourite facies model in the future.

Acknowledgments

This research project was conducted in the framework of the FWO grant “Contourite 3D” (project number 1.5.247.13N) and was assisted by “*The Drifters Research Group*” of the Royal Holloway University of London (UK). The cores and the physical and geochemical analyses on them were acquired in the framework of the following projects: CTM 2012-39599-C03, CTM2008-06399-CO4-02/MAR, CTM2016-75129-C3-1-R and CGL2016-80445-R. The authors want to thank Prof. Dr. E. Achten and Claire Schepens of the Radiology unit of the Ghent University Hospital (UZ Gent) explicitly for making the CT analyses possible and the excellent support during them. An anonymous reviewer, Jürgen Titschack, Mathieu J. Duchesne, Bernard Dennielou and the editor, Michele Rebesco, improved the manuscript greatly by providing constructive reviews. Their critical assessment lifted the paper to a higher level.

References

Agnihotri, R., Altabet, M.A., Herbert, T.D., Tierney, J.E., 2008. Subdecadally resolved paleoceanography of the Peru margin during the last two millennia. Geochem. Geophys. Geosyst. 9, Q05013.

Akaike, H., 1998. Information theory and an extension of the maximum likelihood principle. In: Parzen, E., Tanabe, K., Kitagawa, G. (Eds.), Selected Papers of Hirotugu Akaike. Springer New York, New York, NY, pp. 199–213.

Almeida, E.S.d., Rangayyan, R.M., Marques, P.M.d.A., 2015. Gaussian mixture modeling for statistical analysis of features of high-resolution CT images of diffuse pulmonary diseases. In: 2015 IEEE International Symposium on Medical Measurements and Applications (MeMeA) Proceedings, pp. 1–5.

Alonso, B., 2010. Informe De La Campaña SAGAS bis (SDG-017). B/O Sarmiento De Gamboa 9–25 de Junio de 2010.

Alonso, B., López González, N., Bozzano, G., Casas, D., Ercilla, G., Juan, C., Estrada, F., García, M., Vázquez, J.T., Cacho, I., Palomino, D., d'Acremont, E., El Moumni, B., MONTERA and MOWER teams, 2014. Djibouti Ville Drift (SW Mediterranean): Sedimentation and record of bottom-current fluctuations during the Pleistocene and Holocene. In: Van Rooij, D. (Ed.), 2nd Deep-Water Circulation Congress. VLIZ Special Publication, Ghent, Belgium, pp. 93–94.

Bahr, A., Jiménez-Espejo, F.J., Kolasinac, N., Grunert, P., Hernández-Molina, F.J., Röhl, U., Voelker, A.H.L., Escutia, C., Stow, D.A.V., Hodell, D., Alvarez-Zarikian, C.A., 2014. Deciphering bottom current velocity and paleoclimate signals from contourite deposits in the Gulf of Cdiz during the last 140 kyr: an inorganic geochemical approach. Geochem. Geophys. Geosyst. 15, 3145–3160.

Bertrand, S., Hughen, K.A., Sepúlveda, J., Pantoja, S., 2012. Geochemistry of surface sediments from the fjords of Northern Chilean Patagonia (44–47S): Spatial variability and implications for paleoclimate reconstructions. Geochim. Cosmochim. Acta 76, 125–146.

Borenäs, K.M., Wåhlin, A.K., Ambar, I., Serra, N., 2002. The Mediterranean outflow splitting—a comparison between theoretical models and CANIGO data. Deep-Sea Res. II Top. Stud. Oceanogr. 49, 4195–4205.

Brabant, L., Vlassenbroeck, J., Witte, Y.D., Cnudde, V., Boone, M.N., Dewanckele, J., Hoorebeke, L.V., 2011. Three-dimensional analysis of high-resolution X-ray computed tomography data with morpho+. Microsc. Microanal. 17, 252–263.

Brackenridge, R., Stow, D., Hernández-Molina, F., Jones, C., Mena, A., Alejo, I., Ducassou, E., Llave, E., Ercilla, G., Nombela, M., Pérez-Arlucea, M., Francés, G., 2018. Textural characteristics and facies of sand-rich contourite depositional systems. Sedimentology 65, 2223–2252. https://doi.org/10.1111/sed.12463.

Brackenridge, R.E., Hernández-Molina, F.J., Stow, D.A.V., Llave, E., 2013. A Pliocene mixed contourite–turbidite system offshore the Algarve margin, Gulf of Cadiz: Seismic response, margin evolution and reservoir implications. Mar. Pet. Geol. 46, 36–50.

Branckart, J.M., Pinardi, M., 2001. Abrupt cooling of the Mediterranean Levantine intermediate water at the beginning of the 1980s: observational evidence and model simulation. J. Phys. Oceanogr. 31, 2307–2320.

Cnudde, V., Boone, M.N., 2013. High-resolution X-ray computed tomography in geosciences: a review of the current technology and applications. Earth Sci. Rev. 123, 1–17.

Collart, T., 2019. Scripts in python and R to analyse DICOM CT scans of sediment cores: Published version. https://doi.org/10.5281/zenodo.3386203.

Ercilla, G., Baraza, J., Alonso, B., Estrada, F., Casas, D., Farran, M., 2002. The Ceuta Drift, Alboran Sea, southwestern Mediterranean. In: Stow, D., Pudsey, C., Howe, J., Faugères, J., Viana, A. (Eds.), Deep-water Contourite Systems: Modern Drifts and Ancient Series, Seismic and Sedimentary Characteristics. Geological Society London Memoirespp. 155–170.

Ercilla, G., Juan, C., Hernández-Molina, F.J., Bruno, M., Estrada, F., Alonso, B., Casas, D., Farran, M.l., Llave, E., García, M., Vázquez, J.T., D'Acremont, E., Gorini, C., Palomino, D., Valencia, J., El Moumni, B., Ammar, A., 2016. Significance of bottom currents in deep-sea morphodynamics: an example from the Alboran Sea. Mar. Geol. 378, 157–170.

Fabrés, J., Calafat, A., Sánchez-Vidal, A., Canals, M., Huessner, S., 2002. Composition and spatio-temporal variability of particle fluxes in theWestern Alboran Gyre, Mediterranean Sea. J. Mar. Syst. 33-34, 432–456.

Faugères, J.C., Stow, D.A.V., 2008. Contourite drifts: nature, evolution and controls. In: Rebesco, M., Camerlenghi, A. (Eds.), Contourites. Elsevier, pp. 259–288.

Faugères, J.-C., Gonthier, E., Stow, D.A.V., 1984. Contourite drift molded by deep Mediterranean outflow. Geology 12, 296–300.

Freeman, T., 2010. The Mathematics of Medical Imaging: A Beginner's Guide, Undergraduate Texts in Mathematics and Technology. Springer.

García, M., 2002. Caracterización morfológica del sistema de canales y valles submarinos del talud medio del Golfo de Cádiz (SO de la Peninsula Iberica): Implecaciones oceanográficas. Facultad de Ciencias de l Mar. Univ. Cádiz, Cádiz, pp. 114.

García, M., Hernández-Molina, F.J., Llave, E., Stow, D.A.V., Léon, R., Fernández-Puga, M.C., Diaz del Río, V., Somoza, L., 2009. Contourite erosive features caused by the Mediterranean Outflow Water in the Gulf of Cadiz: Quaternary tectonic and oceanographic implications. Mar. Geol. 257, 24–40.

Gonthier, E.G., Faugères, J.-C., Stow, D.A.V., 1984. Contourite facies of the Faro Drift, Gulf of Cadiz. Geol. Soc. Lond., Spec. Publ. 15, 275–292.

Grant, K., Raupach, R., 2012. SAFIRE: Sinogram Affirmed Iterative Reconstruction. SIEMENS white paper. pp. 7.

Hanebuth, T.J.J., Zhang, W., Hofmann, A.L., Löwemark, L.A., Schwenk, T., 2015. Oceanic density fronts steering bottom-current induced sedimentation deduced from a 50 ka contourite-drift record and numerical modeling (off NW Spain). Quat. Sci. Rev. 112, 207–225.

Henrich, R., Cherubini, Y., Meggers, H., 2010. Climate and sea level induced turbidite activity in a canyon system offshore the hyperarid Western Sahara (Mauritania): the Timiris Canyon. Mar. Geol. 275, 178–198.
Hernández-Molina, F.J., 2009. Los Sistemas Deposicionales Contorníticos: ejemplos alrededor del Margen Ibérico. In: Flor Rodríguez, G., Gallastegui, J., Flor Blanco, G., Martín Llaneza, J. (Eds.), Nuevas contribuciones al margen Ibérico Atlántico 2009, Oviedo, pp. xxi–xxiv.
Hernández-Molina, F.J., Llave, E., Stow, D.A.V., Garciá, m., Somoza, L., Vázquez, J.T., Lobo, F.J., Maestro, A., Díaz del Río, G., León, R., Medialdea, T., Gardner, J., 2006. The contourite depositional system of the Gulf of Cádiz: a sedimentary model related to the bottom current activity of the Mediterranean outflow water and its interaction with the continental margin. Deep-Sea Res. II Top. Stud. Oceanogr. 53, 1420–1463.
Hernández-Molina, F.J., Stow, D.A.V., Alvarez-Zarikian, C.A., Acton, G., Bahr, A., Balestra, B., Ducassou, E., Flood, R., Flores, J.-A., Furota, S., Grunert, P., Hodell, D., Jimenez-Espejo, F., Kim, J.K., Krissek, L., Kuroda, J., Li, B., Llave, E., Lofi, J., Lourens, L., Miller, M., Nanayama, F., Nishida, N., Richter, C., Roque, C., Pereira, H., Sanchez Goñi, M.F., Sierro, F.J., Singh, A.D., Sloss, C., Takashimizu, Y., Tzanova, A., Voelker, A., Williams, T., Xuan, C., 2014. Onset of Mediterranean outflow into the North Atlantic. Science 344, 1244–1250.
Hernández-Molina, F.J., Sierro, F.J., Llave, E., Roque, C., Stow, D.A.V., Williams, T., Lofi, J., Van der Schee, M., Arnáiz, A., Ledesma, S., Rosales, C., Rodríguez-Tovar, F.J., Pardo-Igúzquiza, E., Brackenridge, R.E., 2016. Evolution of the gulf of Cadiz margin and southwest Portugal contourite depositional system: Tectonic, sedimentary and paleoceanographic implications from IODP expedition 339. Mar. Geol. 377, 7–39.
Jiménez-Espejo, F.J., Martínez-Ruiz, F., Finlayson, C., Paytan, A., Sakamoto, T., Ortega-Huertas, M., Finlayson, G., Iijima, K., Gallego-Torres, D., Fa, D., 2007. Climate forcing and Neanderthal extinction in Southern Iberia: insights from a multiproxy marine record. Quat. Sci. Rev. 26, 836–852.
Juan, C., Ercilla, G., Javier Hernández-Molina, F., Estrada, F., Alonso, B., Casas, D., García, M., Farran, M.l., Llave, E., Palomino, D., Vázquez, J.-T., Medialdea, T., Gorini, C., D'Acremont, E., El Moumni, B., Ammar, A., 2016. Seismic evidence of current-controlled sedimentation in the Alboran Sea during the Pliocene and Quaternary: Palaeoceanographic implications. Mar. Geol. 378, 292–311.
Ketcham, R.A., Carlson, W.D., 2001. Acquisition, optimization and interpretation of X-ray computed tomographic imagery: applications to the geosciences. Comput. Geosci. 27, 381–400.
Lebreiro, S., Anton, L., Reguera, M.I., Marzocchi, A., 2018. Paleoceanographic and climatic implications of a new Mediterranean Outflow branch in the southern Gulf of Cadiz. Quat. Sci. Rev. 197, 92–111.
Llave, E., Hernández-Molina, F.J., Somoza, L., Díaz-del-Río, V., Stow, D.A.V., Maestro, A., Alveirinho Dias, J.M., 2001. Seismic stacking pattern of the Faro-Albufeira contourite system (Gulf of Cadiz): a Quaternary record of paleoceanographic and tectonic influences. Mar. Geophys. Res. 22, 487–508.
Llave, E., Schönfeld, J., Hernández-Molina, F.J., Mulder, T., Somoza, L., Díaz del Río, V., Sánchez-Almazo, I., 2006. High-resolution stratigraphy of the Mediterranean outflow contourite system in the Gulf of Cadiz during the late Pleistocene: the impact of Heinrich events. Mar. Geol. 227, 241–262.
Llave, E., Hernández-Molina, F.J., Somoza, L., Stow, D.A.V., Díaz del Río, V., 2007. Quaternary evolution of the contourite depositional system in the Gulf of Cadiz. Geol. Soc. Lond., Spec. Publ. 276, 49–79.
López-González, N., Alonso, B., Juan, C., Ercilla, G., Bozzano, G., Cacho, I., Casas, D., Palomino, D., VÃ¡zquez, J.T., Estrada, F., Bárcenas, P., d'Acremont, E., Gorini, C., El Moumni, B., 2019. 133.000 years of sedimentary record in a contourite drift in the western Alboran Sea: sediment sources and paleocurrent reconstruction. Geosciences 9.
Louarn, E., Morin, P., 2011. Antarctic intermediate water influence on Mediterranean sea water outflow. Deep-Sea Res. I Oceanogr. Res. Pap. 58, 932–942.
Lucchi, R.G., Rebesco, M., Camerlenghi, A., Busetti, M., Tomadin, L., Villa, G., Persico, D., Morigi, C., Bonci, M.C., Giorgetti, G., 2002. Mid-late Pleistocene glacimarine sedimentary processes of a high-latitude, deep-sea sediment drift (Antarctic Peninsula Pacific margin). Mar. Geol. 189, 343–370.
McCave, I.N., 2008. Size sorting during transport and deposition of fine sediments: sortable silt and flow speed. Dev. Sedimentol. 60, 379–407.
McCave, I.N., Hall, I.R., 2006. Size sorting in marine muds: processes, pitfalls and prospects for paleoflow-speed proxies. Geochem. Geophys. Geosyst. 7https://doi.org/10.1029/2006GC001284. Q10N05.
McCave, I.N., Manighetti, B., Robinson, S.G., 1995. Sortable silt and fine sediment size/composition slicing: Parameters for palaeocurrent speed and palaeoceanography. Paleoceanography 10, 593–610.
Mena, A., Francés, G., Pérez-Arlucea, M., Aguiar, P., Barreiro-Vázquez, J.D., Iglesias, A., Barreiro-Lois, A., 2015. A novel sedimentological method based on CT-scanning: use for tomographic characterization of the Galicia Interior Basin. Sediment. Geol. 321, 123–138.
Mena, A., Francés, G., Pérez-Arlucea, M., Hanebuth, T.J.J., Bender, V.B., Nombela, M.A., 2018. Evolution of the Galicia Interior Basin over the last 60 ka: sedimentary processes and palaeoceanographic implications. J. Quat. Sci. 33, 536–549.
Millot, C., 1999. Circulation in the Western Mediterranean Sea. J. Mar. Syst. 20, 423–442.
Millot, C., 2009. Another description of the Mediterranean Sea outflow. Prog. Oceanogr. 82, 101–124.
Mulder, T., Hassan, R., Ducassou, E., Zaragosi, S., Gonthier, E., Hanquiez, V., Marchès, E., Toucanne, S., 2013. Contourites in the Gulf of Cadiz: a cautionary note on potentially ambiguous indicators of bottom current velocity. Geo-Mar. Lett. 33, 357–367.
Mutti, E., Carminati, M., 2012. Deep-water sands of the Brazilian offshore basins. In: AAPG Search and Discovery, article 30219. http://www.searchanddiscovery.com/documents/2012/30219mutti/ndx_mutti.pdf.
Nelson, H.C., Baraza, J., Maldonado, A., 1993. Mediterranean undercurrent sandy contourites, Gulf of Cadiz, Spain. Sediment. Geol. 82, 103–131.
Nizou, J., Hanebuth, T.J.J., Vogt, C., 2011. Deciphering signals of late Holocene fluvial and aeolian supply from a shelf sediment depocentre off Senegal (north-west Africa). J. Quat. Sci. 26, 411–421.
Orsi, T.H., Anderson, A.L., 1999. Bulk density calibration for X-ray tomographic analyses of marine sediments. Geo-Mar. Lett. 19, 270–274.
Palomino, D., Vázquez, J.-T., Ercilla, G., Alonso, B., López-González, N., Díaz-del-Río, V., 2011. Interaction between seabed morphology and water masses around the seamounts on the Motril Marginal Plateau (Alboran Sea, Western Mediterranean). Geo-Mar. Lett. 31, 465–479.
Parilla, G., Kinder, T.H., Preller, R.H., 1986. Deep and intermediate mediterranean water in the western Alboran Sea. Deep Sea Res. Part A 55–88.
Pawlowsky-Glahn, V., Buccianti, A., 2011. Compositional Data Analysis: Theory and Applications. Wiley, West Sussex.
Pedersen, T.F., Shimmield, G.B., N.B. P., 1992. Lack of enhanced preservation of organic matter in sediments under the oxygen minimum on the Oman Margin. Geochim. Cosmochim. Acta 56, 545–551.
Piper, D., Normark, W., 2009. Processes that initiate turbidity currents and their influence on turbidites: a marine geology perspective. J. Sediment. Res. 79, 347–362.
Rebesco, M., Richard, C.S., Cocks, L.R.M., Ian, R.P., 2005. Sedimentary Environments: Contourites, Encyclopedia of Geology. Elsevier, Oxford, pp. 513–528.
Rebesco, M., Wåhlin, A., Laberg, J.S., Schauer, U., Beszczynska-Möller, A., Lucchi, R.G., Noormets, R., Accettella, D., Zarayskaya, Y., Diviacco, P., 2013. Quaternary contourite drifts of the Western Spitsbergen margin. Deep-Sea Res. I Oceanogr. Res. Pap. 79, 156–168.
Rebesco, M., Hernández-Molina, F.J., van Rooij, D., Wåhlin, A., 2014. Contourites and associated sediments controlled by deep-water circulation processes: State of the art and future considerations. Mar. Geol. 352, 111–154.
Rebesco, M., 2004. Numerical Evaluation of Diffuse Spectral Reflectance Data and Correlation with Core Photos, ODP Site 1165, Wild Drift, Cooperation Sea, Antarctica. Proc. Ocean Drill. Program Sci. Results 188, 1–27.
Roberson, S., Weltje, G.J., 2014. Inter-instrument comparison of particle-size analysers. Sedimentology 61, 1157–1174.
Rodríguez-Tovar, F.J., Hernández-Molina, F.J., 2018. Ichnological analysis of contourites: past, present and future. Earth Sci. Rev. 182, 28–41.
Rothwell, R.G., Croudace, I.W., 2015. Twenty years of XRF Core Scanning Marine Sediments: What do Geochemical Proxies tell Us? In: Croudace, I.W., Rothwell, R.G. (Eds.), Micro-XRF Studies of Sediment Cores: Applications of a Non-destructive Tool for the Environmental Sciences. Springer Science, Dordrecht.
Rothwell, R.G., Rack, F.R., 2006. New techniques in sediment core analysis: an introduction. Geol. Soc. Lond., Spec. Publ. 267, 1–29.
Sánchez-Leal, R.F., Bellanco, M.J., Fernández-Salas, L.M., García-Lafuente, J., Gasser-Rubinat, M., González-Pola, C., Hernández-Molina, F.J., Pelegrí, J.L., Peliz, A., Relvas, P., Roque, D., Ruiz-Villarreal, M., Sammartino, S., Sánchez-Garrido, J.C., 2017. The Mediterranean Overflow in the Gulf of Cadiz: a rugged journey. Sci. Adv. 3, eaao0609.
Sansom, P., 2018. Hybrid turbidite-contourite systems of the Tanzanian margin. Pet. Geosci. 2018–2044.
Schultheiss, P.J., Weaver, P.P.E., 1992. Multi-sensor logging for science and industry. In: Proceedings of Ocean '92, Mastering the Oceans Through Technology, pp. 608–613 New-port, Rhode Island.
Shanmugam, G., 2000. 50 years of the turbidite paradigm (1950s–1990s): deep-water processes and facies models—a critical perspective. Mar. Pet. Geol. 17, 285–342.
Shanmugam, G., 2008. Chapter 5 deep-water bottom currents and their deposits. In: Rebesco, M., Camerlenghi, A. (Eds.), Developments in Sedimentology. Elsevier, pp. 59–81.
Shanmugam, G., 2012. New perspectives on deep-water sandstones: origin, recognition, initiation and reservoir quality. In: Handbook of Petroleum Exploration and Production. Elsevier, Amsterdam.
Southard, J.B., Cacchione, D.A., 1975. Bed configurations. In: Harms, J.C., Southard, J.B., Spearing, D.R., Walker, R.G. (Eds.), Depositional Environments as Interpreted From Primary Sedimentary Structures and Stratification Sequences. Lecture Notes for Society of Economic Paleontologists and Mineralogists Short Course no. 2pp. 5–43 Dallas, Texas.
Spofforth, D.J.A., Pälike, H., Green, D., 2008. Paleogene record of elemental concentrations in sediments from the Arctic Ocean obtained by XRF analyses. Paleoceanography 23.
Stow, D.A.V., Faugères, J.C., 2008. Chapter 13 contourite facies and the facies model. In: Rebesco, M., Camerlenghi, A. (Eds.), Developments in Sedimentology. Elsevier, pp. 223–256.
Stow, D.A.V., Faugères, J.-C., Gonthier, E., 1986. Facies distribution and textural variation in Faro Drift contourites: Velocity fluctuation and drift growth. Mar. Geol. 72, 71–100.
Stow, D.A.V., Faugères, J.-C., Howe, J.A., Pudsey, C.J., Viana, A.R., 2002. Bottom currents, contourites and deep-sea sediment drifts: current state-of-the-art. Geological Society, London, Memoirs 22, 7–20.
Stow, D.A.V., Hernández-Molina, F.J., Llave, E., Sayago-Gil, M., Díaz del Río, V., Branson, A., 2009. Bedform-velocity matrix: the estimation of bottom current velocity from bedform observations. Geology 37, 327–330.
Stow, D.A.V., Hernández-Molina, F.J., Llave, E., Bruno, M., García, M., Díaz del Rio, V., Somoza, L., Brackenridge, R.E., 2013. The Cadiz Contourite Channel: sandy contourites, bedforms and dynamic current interaction. Mar. Geol. 343, 99–114.
Thomson, J., Croudace, I.W., Rothwell, R.G., 2006. A geochemical application of the ITRAX scanner to a sediment core containing eastern Mediterranean sapropel units. Geol. Soc. Lond., Spec. Publ. 267, 65–77.
Tjallingii, R., Stattegger, K., Wetzel, A., Van Phach, P., 2010. Infilling and flooding of the

Mekong River incised valley during deglacial sea-level rise. Quat. Sci. Rev. 29, 1432–1444.
Vázquez, J.T., Alonso, B., 2012. Informe Científico – Técnico Campaña Montera-0412. 23 de Abril a 15 de Mayo 2012, b/o Sarmiento De Gamboa.
Verdicchio, G., Trincardi, F., 2008. Shallow-water contourites. In: Rebesco, M., Camerlenghi, A. (Eds.), Contourites. Developments in Sedimentology Elsevier, pp. 409–433.
Viana, A.R., Faugères, J.C., Stow, D.A.V., 1998. Bottom-current-controlled sand deposits—a review of modern shallow- to deep-water environments. Sediment. Geol. 115, 53–80.
Weltje, G.J., Tjallingii, R., 2008. Calibration of XRF core scanners for quantitative geochemical logging of sediment cores: Theory and application. Earth Planet. Sci. Lett. 274, 423–438.
Zatz, I.M., 1981. Basic principles of computed tomography scanning. In: Newton, T.H., Potts, D.G. (Eds.), Radiology of the Skull and Brain, (Mosby, St. Louis).